



Highly sensitive strain sensor based on composite interference established within S-tapered multimode fiber structure

Ke Tian, Meng Zhang, Gerald Farrell, Ruoning Wang, ELFED LEWIS, Pengfei Wang

Publication date

01-01-2018

Published in

Optics Express;26 (26), pp. 33982-33992

Licence

This work is made available under the [CC BY-NC-SA 1.0](#) licence and should only be used in accordance with that licence. For more information on the specific terms, consult the repository record for this item.

Document Version

1

Citation for this work (HarvardUL)

Tian, K., Zhang, M., Farrell, G., Wang, R., LEWIS, E. and Wang, P. (2018) 'Highly sensitive strain sensor based on composite interference established within S-tapered multimode fiber structure', available: <https://hdl.handle.net/10344/7470> [accessed 23 Jul 2022].

This work was downloaded from the University of Limerick research repository.

For more information on this work, the University of Limerick research repository or to report an issue, you can contact the repository administrators at ir@ul.ie. If you feel that this work breaches copyright, please provide details and we will remove access to the work immediately while we investigate your claim.



Highly sensitive strain sensor based on composite interference established within S-tapered multimode fiber structure

KE TIAN,¹ MENG ZHANG,¹ GERALD FARRELL,² RUONING WANG,¹ ELFED LEWIS,³ AND PENGFEI WANG^{1,4,*}

¹Key Laboratory of In-fiber Integrated Optics of Ministry of Education, College of Science, Harbin Engineering University, Harbin 150001, China

²Photonics Research Centre, Dublin Institute of Technology, Kevin Street, Dublin 8, Ireland

³Optical Fibre Sensors Research Centre, Department of Electronic and Computer Engineering, University of Limerick, Limerick, Ireland

⁴Key Laboratory of Optoelectronic Devices and Systems of Ministry of Education and Guangdong Province, College of Optoelectronic Engineering, Shenzhen University, Shenzhen 518060, China

*pengfei.wang@dit.ie

Abstract: In this paper, a novel strain sensor based on composite interference established within an S-tapered multimode (STM) fiber structure is proposed and experimentally demonstrated. The STM fibre structure is simply realized by non-axially tapering a traditional single-mode-multimode-single-mode (SMS) fiber into S-shape using a fusion splicer. This fabricated S-tapered structure provides an extra Mach-Zehnder interferometer (MZI) that is introduced within the multimode fibre (MMF) section; therefore, composite interference based on the inherent multimode interference (MMI) of an SMS and the introduced MZI is successfully established. This resultant composite interference greatly enhances the performance of traditional SMS fibre structures for strain sensing, with a maximum strain measurement sensitivity as high as $-103.8 \text{ pm}/\mu\epsilon$ achieved with a detectable strain resolution of $0.2 \mu\epsilon$. Benefiting from the experimentally determined high sensitivity and good repeatability, this low-cost strain sensor can be realistically applied in many areas where high accuracy strain measurement is required.

© 2018 Optical Society of America under the terms of the [OSA Open Access Publishing Agreement](#)

1. Introduction

Strain measurement plays an important role in structural health monitoring (SHM) for many civil structures such as dams, bridges, highways, towers, etc., and various strain sensors have been investigated to meet the need for high accuracy strain measurement, particularly within some specialist fields such as aerospace, clinical and micromachining. Among the existing strain sensor technologies, optical fibre based strain sensors have attracted much research attention due to their unique advantages which include being lightweight, compact, stable in hostile environments, and possessing an inherent immunity to external electromagnetic interference. To date, fibre optic strain sensors have been successfully developed based on fibre gratings [1–4], Mach-Zehnder interferometers (MZIs) [5–8], Fabry-Perot interferometers (FPIs) [9–11] and Sagnac interferometers [12,13]. However, for those configurations, the fabrication processes are relatively complicated which requires pricy fabrication devices and results in a time-consuming of fabrication process, but with the strain measurement resolutions are still not well suited in many high accuracy measurement fields.

Multimode interference (MMI), a well-established phenomenon that can exist in multimode waveguides, has been widely explored and applied in telecommunications [14,15]. A very common form of MMI device which has also been intensively investigated, is a single-mode-multimode-single-mode (SMS) fibre structure. In the optical fibre sensing field, SMS fibre structures have been proven to be able to develop as the basis of sensors for a

variety of measurands, e.g. temperature [16], displacement [17], curvature [18,19], refractive index (RI) [20], humidity [21] and magnetic field strength [22,23]. Given that the underlying operating principle of SMS fibre structures is MMI and since applied strain will alter the conditions for MMI in a repeatable manner, thus strain measurement can also be implemented using an SMS fibre structure. For example, a strain sensor has been reported based on a graded-index MMF fabricated SMS fibre structure [24]. However, since the length of MMF used is up to 1.8 m, this sensor is not compact which greatly limits its application. The larger Young's Modulus of polymer fibre allows for a larger range of strain measurement and this has been successfully used in an polymer MMF based SMS fibre structure, for which the detection range can reach $2 \times 10^4 \mu\epsilon$ [25]. However, due to the high thermal-optical coefficient of polymer fibre, this sensor has a relatively high temperature-strain crosstalk circa $33 \mu\epsilon/^\circ\text{C}$. In previous work undertaken by some of the authors of this article, a quasi F-P cavity was embedded within a SMS fibre structure and was proven to offer double the strain sensitivity compared to traditional SMS fibre structures [26]. However, its limited strain sensitivity is still deemed unsatisfactory for many measurement applications. Therefore, there exists a clear need for a higher sensitivity strain sensor to allow for high accuracy measurements.

In this paper, we demonstrate a high sensitivity strain sensor based on composite interference established within an S-tapered multimode (STM) fibre structure. The STM fibre structure is simply realized by non-axially tapering a traditional SMS fibre into S-shape using a fusion splicer. Owing to the fabricated S-tapered structure, an extra MZI is introduced within the MMF section, and composite interference based on the inherent MMI and the introduced MZI is successfully established. This resultant composite interference generates two available interference dips in the wavelength range of 1450-1600 nm, and a maximum strain measurement sensitivity of $-103.8 \text{ pm}/\mu\epsilon$ is achieved experimentally with a detectable strain resolution of $0.2 \mu\epsilon$. In addition, the temperature response characteristics of this sensor are also investigated. By monitoring the variation of the two dips in the wavelength domain, simultaneous measurement of strain and temperature is also achieved to overcome the temperature induced cross-sensitivity.

2. Principle and fabrication

Figure 1 illustrates the light propagation principle within the STM fibre structure. As depicted in Fig. 1, in a fashion similar to a traditional SMS structure, the STM fibre structure consists of two input/output SMFs and an MMF, but with the MMF section formed in an S-shaped tapered area.

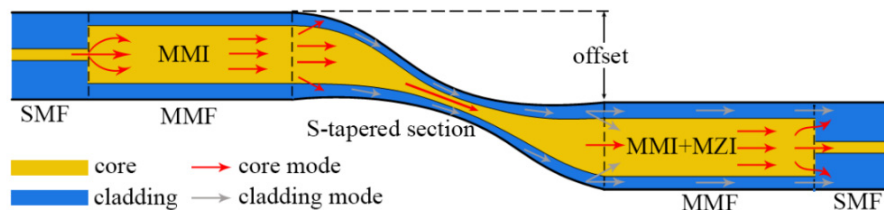


Fig. 1. Schematic diagram of the light propagation within the STM fibre structure.

The light from the source initially propagates along the core of the input SMF in the fundamental mode (LP_{01}). When the light launches into the MMF section, a series of high-order modes (LP_{0m}) are effectively excited due to the mode field mismatch between the SMF and MMF. For a step-index MMF, the excited mode number M can be approximately calculated by:

$$M \approx \frac{2a\sqrt{n_{co}^2 - n_{cl}^2}}{\lambda} \quad (1)$$

where a is the radius of the MMF core, n_{co} and n_{cl} are the RI for the MMF core and cladding, respectively, and λ is the free space wavelength. As the light propagates within the MMF section, the electric field distribution $E(r, z)$ at the propagation distance z can be expressed as [27]:

$$E(r, z) = \sum_{m=1}^M e_m F_m(r) \exp(i\beta_m z) \quad (2)$$

where $F_m(r)$ is the field profile of LP_{0m} excited within the MMF, β_m is the propagation constant of the excited m^{th} order mode and e_m is the excitation coefficient which can be calculated using the following formula:

$$e_m = \frac{\int_0^\infty E(r, 0) F_m(r) r dr}{\int_0^\infty F_m(r) F_m(r) r dr} \quad (3)$$

When the light arrives at the S-tapered section, due to the S-shaped geometry, a portion of light from the MMF core is coupled into the MMF cladding at which point it excites cladding modes [28]. These excited cladding modes propagate within the S-tapered MMF cladding, and when they transmit through the S-tapered section, a portion of the cladding modes are recoupled back into the MMF core. Due to the differences in effective RIs between the core and the cladding and the optical path difference of the light signals in transmission, interference between the cladding modes and the modes propagating in the core occurs and thus an MZI is formed. Considering a typical two-mode MZI, the phase difference φ^{mn} between the m^{th} order core mode and n^{th} order cladding mode can be expressed as follows [29]:

$$\varphi^{mn} = \frac{2\pi(n_{co}^m - n_{cl}^n)L_{eff}}{\lambda} \quad (4)$$

where n_{co}^m and n_{cl}^n are the effective RIs of the m^{th} order core mode and n^{th} order cladding mode respectively, and L_{eff} is the effective interference length. When the phase difference meets the condition of $\varphi^{mn} = (2s + 1)\pi$, $s = 0, 1, 2, \dots$, the location of the attenuation dip wavelength can be determined by [30]:

$$\lambda_s = \frac{2(n_{co}^m - n_{cl}^n)L_{eff}}{2s + 1} \quad (5)$$

Therefore, at the second MMF section, each mode is associated with their respective phase difference and MMI between each mode occurs again, hence resulting in composite interference. Eventually, when the light arrives at the interface of the output SMF, a portion of light is coupled into the core of the output SMF, while the remainder is coupled into the cladding and finally lost over a short distance. When strain is applied at both ends of the SMF, the axial offset of the S-tapered structure would be varied as depicted in Fig. 2, which in turn changes the effective interference length L_{eff} and the effective RI of core and cladding modes, and results in a variation of the transmission spectrum.

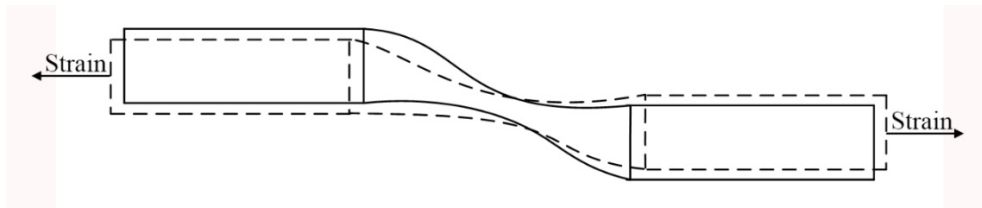


Fig. 2. Schematic diagram of deformation when applied axial strain on the STM fibre structure.

The fabrication process for STM fibre structure is relatively simple, in that the only major instrument required is a conventional fusion splicer (Fujikura, FSM-100P +). Initially, a SMS fibre structure was prepared by sandwiching a 2 cm length MMF (AFS105/125) between two standard SMFs (SMF-28). The 2 cm length of MMF was chosen because it provides a quasi-image distance at the taper point [31], making the coupling of the light between the core and the cladding more efficient. The transmission spectrum of the fabricated SMS fibre structure was measured and is shown in Fig. 3. One of the fibre holders of the fusion splicer was then manually adjusted with a specific axial offset and the centre of the SMS fibre sample was placed between the two fibre holders and fixed. A discharge program was executed on the fusion splicer to achieve the final S-tapered structure. After repeated attempts at various combination of discharge current and discharge time, the optimum discharge current and discharge time were determined to be 10.8 mA and 4000 ms, respectively. By adjusting different axial offsets between the two fibre holders, an STM fibre structure with different axial offsets can be realized. In addition, by changing the discharge time of arc, the taper diameter can also be controlled. In this investigation, considering the mechanical stability of the fibre structure for strain measurement, the diameter of the taper waist was selected to be 40 μm .

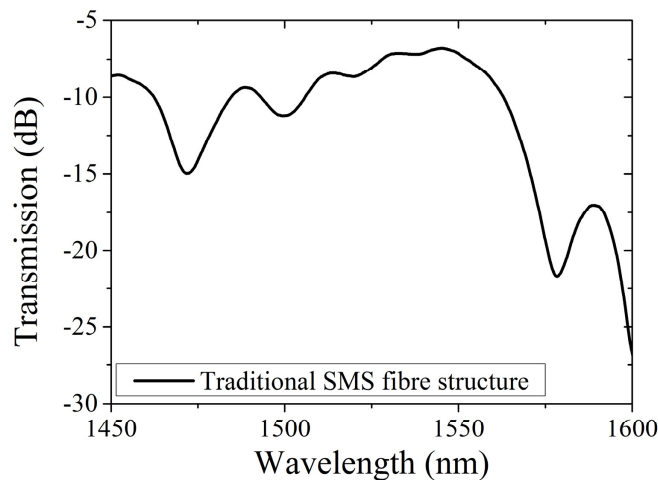


Fig. 3. Transmission spectrum of an untapered SMS fibre structure sandwiched with 2 cm length MMF.

To establish an effective composite interference within the MMF section, an appropriate axial offset needed to be determined. Therefore, the STM fibre structures with different axial offsets were experimentally fabricated. The optical microscopic images and the corresponding transmission spectrums (1450 nm-1600 nm) are shown in Fig. 4. As shown in Fig. 4(a)-4(d), the STM fibre structures were S-tapered with different axial offsets, being 0 μm , 35 μm , 60 μm and 80 μm . From Fig. 4(e)-4(h), it can be observed that as the axial offset increases, the transmission loss of the spectrum increases because more light leaks out of the

fibre in the S-shaped bent area. In the case of Fig. 4(e), the SMS fibre structure was only tapered but without offset, and no obvious interference pattern was detected due to the fact that no MZI was introduced in the MMF section. As analyzed in the principles section, when the MMF is reshaped into S-shape, composite interference can potentially be established. However, in the case of the 35 μm offset, the resultant effect is relatively weak that the composite interference resulting interference dips have a relatively low extinction ratio (ER). By increasing the offset to 60 μm , an enhanced interference pattern was obtained, in which two interference dips, dip A and dip B were observed with good ER (more than 10 dB), with their central wavelengths located at 1491.4 nm and 1533 nm. As the axial offset was further increased to 80 μm , the contrast in the transmission spectrum becomes low. If the axial offset continues to increase, excess light is leaked out the fibre which results in an intolerably large loss. Ultimately, based on the results of the above experiments, an appropriate axial offset to form an effective composite interference should be in the region of 60 μm .

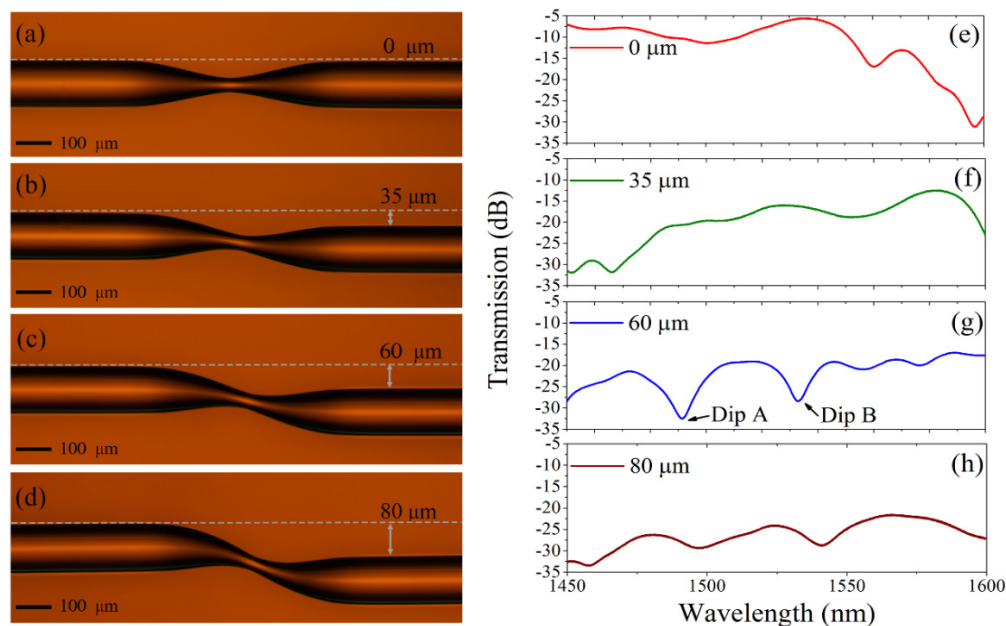


Fig. 4. (a)-(d) Optical microscopic images of the STM fibre structure with different offset values; (e)-(h) Transmission spectrums corresponding to the cases in (a)-(d).

Based on the above theoretical analysis and the determined fabrication parameters in Fig. 4(g), a numerical simulation using the Beam Propagation Method (BPM) has been conducted to describe the optical field distribution within the STM fibre structure. The specific simulation parameters were: the diameter and RI for the MMF core/cladding are 105/125 μm and 1.4446/1.4271. The axial offset, waist diameter of the taper and the length of the S-shape section were 60 μm , 40 μm , 500 μm , respectively. When the free space wavelength was set to 1550 nm, the simulation result is shown in Fig. 5. It is clearly observed that the MMI pattern appears at the first MMF section, and when the light propagates through the S-tapered area, most of light is coupled into the core and cladding of second MMF, while a small portion of the light leaks out of the fibre. Hence composite interference based on MMI and MZI occurs at the second MMF section. Ultimately, a portion of light from the MMF is coupled into the core of the output SMF which can be detected by an appropriate interrogation device.

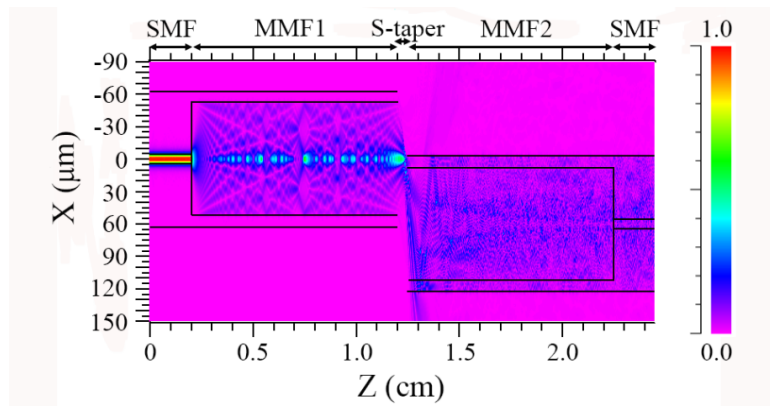


Fig. 5. Simulated optical field intensity distribution within the STM fibre structure at the free space wavelength of 1550 nm.

3. Experiment and discussion

The experimental setup for strain measurement is illustrated in Fig. 6. The STM sample was fixed on the centre of two translation stages. The axial tensile stress applied to the sample was accurately controlled using an in-house developed computer program, such that the two translation stages can be displaced in both directions (positive and negative) along the meridional axes of the SMF. The changed strain value can be calculated using a standard strain calculation formula: $\Delta\varepsilon = \Delta l/l$, where l is the initial distance between two translation stages, and Δl is the imposed displacement (change in length). Broadband light from a supercontinuum source (SC, YSL, China) was coupled into the input SMF of the sample, and the output optical spectral signal was interrogated by a high-resolution (20 pm) optical spectrum analyzer (OSA, YOKOGAWA AQ6370D, Japan).

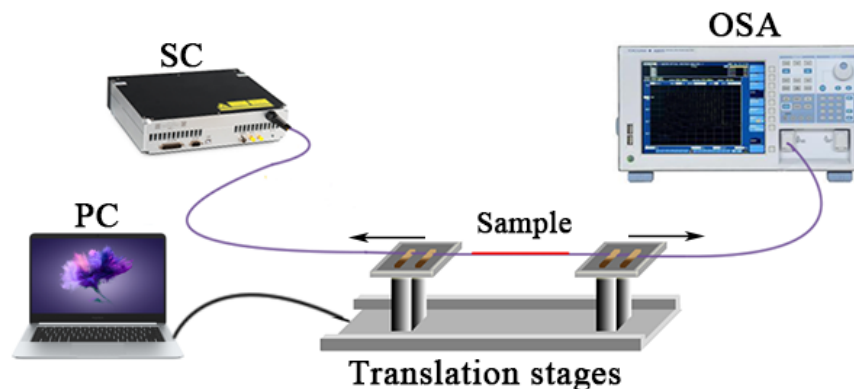


Fig. 6. Schematic diagram of the experimental setup for strain measurement.

Figure 7(a) shows the evolution of the transmission spectrum for dip A and dip B as the applied strain was increased from $0 \mu\epsilon$ to $170 \mu\epsilon$ with an incremental step of $10 \mu\epsilon$. As shown in Fig. 7(a), when the applied strain was increased, both dip A and dip B exhibit a clear blue-shift in the wavelength domain. In order to test the repeatability of the proposed sensor, a reversed measurement cycle was carried out, for which the applied strain was decreased from $170 \mu\epsilon$ back to $0 \mu\epsilon$, and the corresponding transmission spectrum evolution result is shown in Fig. 7(b). It is clear that when the applied strain changed in an inverse direction, the evolution features of dip A and dip B were opposite to the strain increase case, for which the dipoles moved to a longer wavelength direction (red-shift).

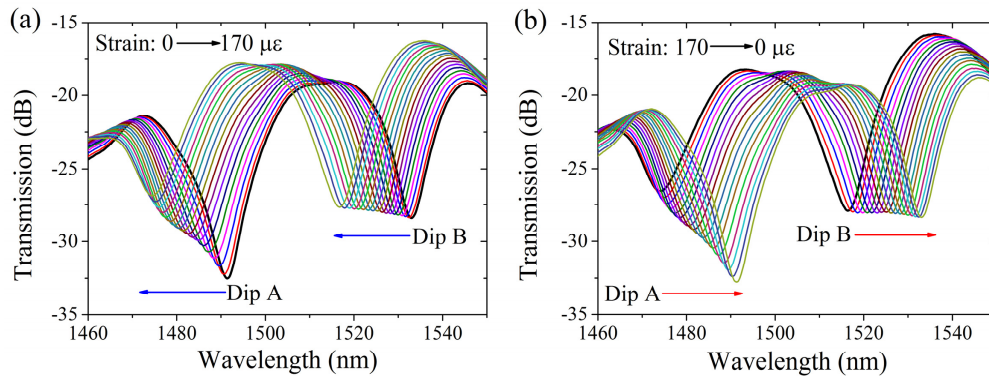


Fig. 7. Transmission spectrum evolution when applied strain is changed (a) strain increases; (b) strain decreases.

The resulting wavelength shifts of the dip A and dip B are plotted and linearly fitted in Fig. 8, for both the strain increase and decrease cases. It can be seen that both the fitting curves exhibit excellent linearity with high linear regression coefficient values (R^2). For dip A, the strain sensitivities in strain increase and decrease processes were calculated to be -103.8 pm/ $\mu\epsilon$ with R^2 of 0.9949 and -104 pm/ $\mu\epsilon$ with R^2 of 0.9960, respectively. For dip B, the strain sensitivities for the strain increase and decrease processes were calculated as -96.5 pm/ $\mu\epsilon$ with R^2 of 0.9959 and -97.3 pm/ $\mu\epsilon$ with R^2 of 0.9958, respectively. Based on the observed transmission spectrum evolution features and the determined sensitivities, it is also demonstrated that there is no hysteresis present and this proposed strain sensor possesses good measurement repeatability because of the minor differences between the results for the strain increase and decrease cases. Furthermore, given the 20 pm resolution of the OSA used in the experiments, the strain measurement resolution of this sensor system was estimated to be 0.2 $\mu\epsilon$, which is a very acceptable value in many strain measurement areas.

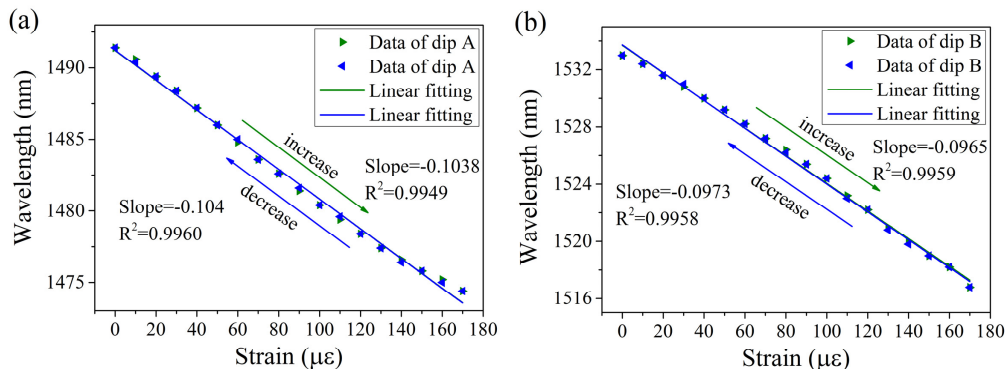


Fig. 8. Linear fitting curves for the dip wavelength shifts against strain variation: (a) dip A; (b) dip B.

To further confirm the enhanced strain sensing performance resulting from the established composite interference, a comparison experiment using a traditional SMS fibre structure with an identical MMF length of 2 cm but without the S-shaped taper was carried out. From the transmission spectrum which is presented in Fig. 3, one interference dip with the centre wavelength of 1578.2 nm was selected as the monitoring target in the strain measurement experiment. Figure 9(a) shows that the monitoring dip exhibits a blue-shift in the wavelength domain when the strain was increased from 0 $\mu\epsilon$ to 1200 $\mu\epsilon$. The resulting wavelength shift of the dip against the strain variation is plotted and fitted in Fig. 9(b). From the fitting results,

the strain sensitivity of the traditional SMS fibre structure was determined to be $-3.07 \text{ pm}/\mu\epsilon$ with R^2 of 0.9751. Through this comparison experiment, it is clear that the strain sensing performance of the traditional SMS fibre structure was significantly improved with the inclusion of the S-taper, with the strain sensitivity of the STM fibre structure almost 33 times higher than the traditional SMS fibre structure.

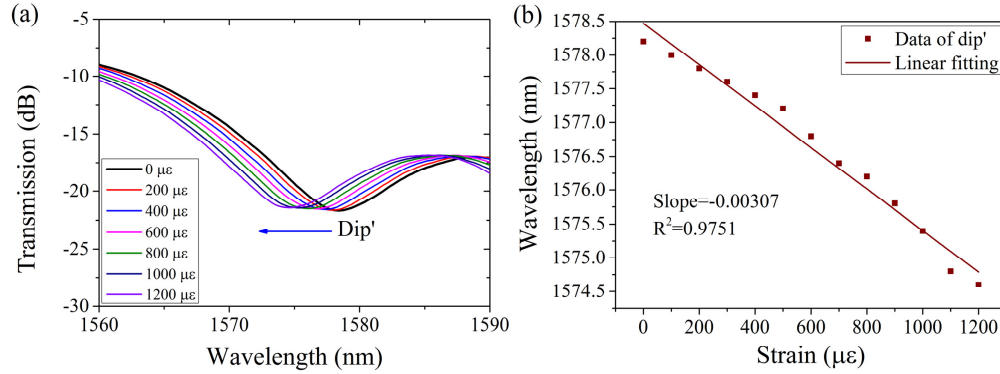


Fig. 9. (a) Transmission spectrum evolution of a traditional SMS fibre structure with 2 cm length MMF when applied strain is changed; (b) linear fitting curve of the dip' wavelength shifts against strain variation.

In addition to the fundamental strain measurement, the temperature response characteristics of the proposed STM fibre structure were also investigated. As shown in Fig. 10(a), both dip A and dip B exhibit a red-shift in wavelength domain when the sensor sample was heated from 30°C to 100°C with a step of 10°C . The temperature induced wavelength shifts of dip A and dip B are plotted and linearly fitted in Fig. 10(b). From the fitting results, the temperature sensitivities of dip A and dip B were determined to be $36.2 \text{ pm}/^\circ\text{C}$ with R^2 of 0.9960 and $25.2 \text{ pm}/^\circ\text{C}$ with R^2 of 0.9893, respectively.

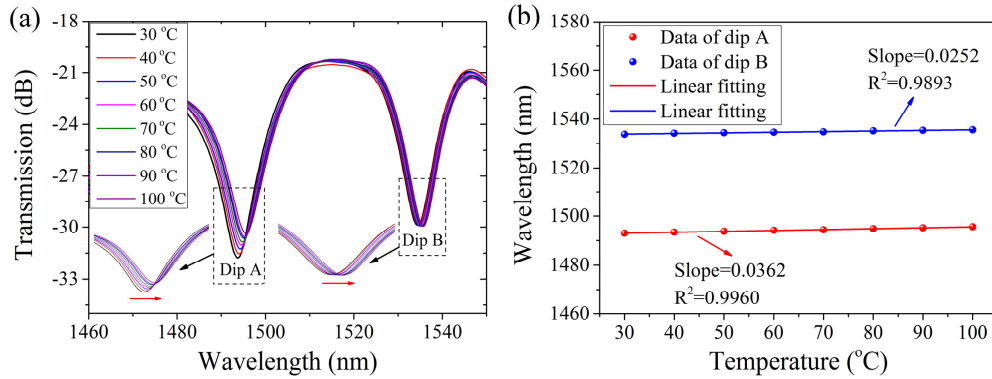


Fig. 10. (a) Transmission spectrum evolution as temperature is changed; (b) linear fitting curve of the dip' wavelength shift against temperature variation.

Since dip A and dip B have different response characteristics for strain and temperature, simultaneous measurement of strain and temperature can also be achieved and thus overcome the temperature induced cross-sensitivity in practical strain measurement. Based on the above obtained sensitivity coefficients, a demodulation matrix is established, which is expressed as:

$$\begin{bmatrix} \Delta\epsilon \\ \Delta T \end{bmatrix} = \begin{bmatrix} -103.8 \text{ pm} / \mu\epsilon & 36.2 \text{ pm} / ^\circ\text{C} \\ -96.5 \text{ pm} / \mu\epsilon & 25.2 \text{ pm} / ^\circ\text{C} \end{bmatrix}^{-1} \begin{bmatrix} \Delta\lambda_A \\ \Delta\lambda_B \end{bmatrix} \quad (6)$$

where $\Delta\varepsilon$, and ΔT represent the variation of strain and temperature, $\Delta\lambda_A$, and $\Delta\lambda_B$ represent the wavelength shifts of dip A and dip B respectively.

Table 1 shows a comparison of the strain sensing performance between the sensor structure described in this investigation and the other configurations cited in this paper. Compared to the previous examples, the sensor in this investigation provides a superior strain sensitivity, and has only a small temperature-strain crosstalk. Moreover, this crosstalk can also be discriminated in practical applications by simultaneously measuring strain and temperature. Therefore, the sensor described in this investigation can be a competitive candidate for use in high accuracy strain measurement fields.

Table 1. Comparison of sensing performance of different strain sensors developed to date

Measurement configuration	Strain sensitivity (pm/ $\mu\varepsilon$)	Temperature-strain crosstalk ($\mu\varepsilon/^\circ\text{C}$)	Simultaneous measurement	Ref.
FBG	0.42	16.67	Yes	1
FBG written in polarization maintaining fibre	1.16	7.93	Yes	2
LPG combined with fibre loop mirror	-4.37	19.45	Yes	3
LPG based on periodically taper	-0.55	90.18	Yes	4
MZI based on few mode multicore fibre	13.96	7.85	Yes	5
MZI based on abrupt taper	2	Not given	No	6
MZI based on inner air cavity	6.8	Not given	No	7
MZI based on helical multicore fibre structure	-61.8	0.42	Yes	8
FPI based on air bubble cavity	3.29	0.33	No	9
FPI based on air cavity	6	0.18	No	10
FPI based on hybrid cavity	5.2	0.25	Yes	11
Sagnac interferometer based on PCF	0.23	1.26	No	12
Sagnac interferometer based on hollow-core PCF	-0.18	22.06	No	13
MMI based on graded-index MMF	18.6	3.15	No	24
MMI based on polymer MMF	-1.72	33	No	25
MMI and FPI	-2.60	2.62	Yes	26
MMI and MZI	-103.8	0.35	Yes	This work

4. Conclusion

In summary, a high sensitivity strain sensor based on composite interference established within an S-tapered multimode (STM) fibre structure has been characterized theoretically and demonstrated experimentally. By non-axially tapering the MMF section of a traditional SMS fibre using a fusion splicer, an S-tapered structure was successfully fabricated. The S-tapered structure provides an extra MZI introduced within the MMF section, therefore composite interference based on the inherent MMI and the introduced MZI is established. This established composite interference greatly enhances the strain measurement sensitivity of traditional SMS fibre structures by a factor of almost 33 times, achieving a maximum sensitivity of -103.8 pm/ $\mu\varepsilon$ with a strain resolution of 0.2 $\mu\varepsilon$. Furthermore, due to availability of two indicators in the wavelength domain, strain and temperature can also be measured simultaneously by this proposed sensor. The clear advantages accruing from the novel design of the sensor in this investigation include high sensitivity, good repeatability, low-cost and strain-temperature discrimination, meaning that it is potentially an excellent candidate for use for high accuracy strain measurement applications.

Funding

National Key R&D Program of China (2016YFE0126500); National Natural Science Foundation of China (NSFC) (61575050); Key Program for Natural Science Foundation of Heilongjiang Province of China (ZD2016012); Open Fund of the State Key Laboratory on Integrated Optoelectronics (IOSKL2016KF03); 111 project (B13015) to the Harbin Engineering University; Ph. D Student Research and Innovation Fund of the Fundamental Research Funds for the Central Universities (HEUGIP201820).

References

1. S. W. James, M. L. Dockney, and R. P. Tatam, "Simultaneous independent temperature and strain measurement using in-fibre Bragg grating sensors," *Electron. Lett.* **32**(12), 1133–1134 (1996).
2. B. Yin, M. Wang, S. Wu, Y. Tang, S. Feng, Y. Wu, and H. Zhang, "Fiber ring laser based on MMF-PMFBG-MMF filter for three parameters sensing," *Opt. Express* **25**(25), 30946–30955 (2017).
3. O. Frazao, L. M. Marques, S. Santos, J. M. Baptista, and J. L. Santos, "Simultaneous Measurement for Strain and Temperature Based on a Long-Period Grating Combined With a High-Birefringence Fiber Loop Mirror," *IEEE Photonics Technol. Lett.* **18**(22), 2407–2409 (2006).
4. M.-S. Yoon, S. Park, and Y.-G. Han, "Simultaneous Measurement of Strain and Temperature by Using a Micro-Tapered Fiber Grating," *J. Lightwave Technol.* **30**(8), 1156–1160 (2012).
5. X. Zhan, Y. Liu, M. Tang, L. Ma, R. Wang, L. Duan, L. Gan, C. Yang, W. Tong, S. Fu, D. Liu, and Z. He, "Few-mode multicore fiber enabled integrated Mach-Zehnder interferometers for temperature and strain discrimination," *Opt. Express* **26**(12), 15332–15342 (2018).
6. Z. Tian and S. S. Yam, "In-Line Abrupt Taper Optical Fiber Mach-Zehnder Interferometric Strain Sensor," *IEEE Photonics Technol. Lett.* **21**(3), 161–163 (2009).
7. C. R. Liao, D. N. Wang, and Y. Wang, "Microfiber in-line Mach-Zehnder interferometer for strain sensing," *Opt. Lett.* **38**(5), 757–759 (2013).
8. H. Zhang, Z. Wu, P. P. Shum, X. Q. Dinh, C. W. Low, Z. Xu, R. Wang, X. Shao, S. Fu, W. Tong, and M. Tang, "Highly sensitive strain sensor based on helical structure combined with Mach-Zehnder interferometer in multicore fiber," *Sci. Rep.* **7**(1), 46633 (2017).
9. Y. Wu, Y. Zhang, J. Wu, and P. Yuan, "Temperature-insensitive fiber optic Fabry-Perot interferometer based on special air cavity for transverse load and strain measurements," *Opt. Express* **25**(8), 9443–9448 (2017).
10. S. Liu, Y. Wang, C. Liao, G. Wang, Z. Li, Q. Wang, J. Zhou, K. Yang, X. Zhong, J. Zhao, and J. Tang, "High-sensitivity strain sensor based on in-fiber improved Fabry-Perot interferometer," *Opt. Lett.* **39**(7), 2121–2124 (2014).
11. A. Zhou, B. Qin, Z. Zhu, Y. Zhang, Z. Liu, J. Yang, and L. Yuan, "Hybrid structured fiber-optic Fabry-Perot interferometer for simultaneous measurement of strain and temperature," *Opt. Lett.* **39**(18), 5267–5270 (2014).
12. X. Dong, H. Y. Tam, and P. Shum, "Temperature-insensitive strain sensor with polarization-maintaining photonic crystal fiber based Sagnac interferometer," *Appl. Phys. Lett.* **90**(15), 151113 (2007).
13. G. Kim, T. Cho, K. Hwang, K. Lee, K. S. Lee, Y.-G. Han, and S. B. Lee, "Strain and temperature sensitivities of an elliptical hollow-core photonic bandgap fiber based on Sagnac interferometer," *Opt. Express* **17**(4), 2481–2486 (2009).
14. W. S. Mohammed, P. W. E. Smith, and X. Gu, "All-fiber multimode interference bandpass filter," *Opt. Lett.* **31**(17), 2547–2549 (2006).
15. A. M. Hatta, Y. Semenova, G. Rajan, and G. Farrell, "Polarization dependence of an edge filter based on singlemode-multimode-singlemode fibre," *Opt. Laser Technol.* **42**(6), 1044–1048 (2010).
16. P. Wang, M. Ding, L. Bo, C. Guan, Y. Semenova, Q. Wu, G. Farrell, and G. Brambilla, "Fiber-tip high-temperature sensor based on multimode interference," *Opt. Lett.* **38**(22), 4617–4620 (2013).
17. A. Mehta, W. Mohammed, and E. G. Johnson, "Multimode interference-based fiber-optic displacement sensor," *IEEE Photonics Technol. Lett.* **15**(8), 1129–1131 (2003).
18. K. Tian, Y. Xin, W. Yang, T. Geng, J. Ren, Y.-X. Fan, G. Farrell, E. Lewis, and P. Wang, "A Curvature Sensor Based on Twisted Single-Mode-Multimode-Single-Mode Hybrid Optical Fiber Structure," *J. Lightwave Technol.* **35**(9), 1725–1731 (2017).
19. O. Frazão, J. Viegas, P. Caldas, J. L. Santos, F. M. Araújo, L. A. Ferreira, and F. Farahi, "All-fiber Mach-Zehnder curvature sensor based on multimode interference combined with a long-period grating," *Opt. Lett.* **32**(21), 3074–3076 (2007).
20. P. Wang, G. Brambilla, M. Ding, Y. Semenova, Q. Wu, and G. Farrell, "High-sensitivity, evanescent field refractometric sensor based on a tapered, multimode fiber interference," *Opt. Lett.* **36**(12), 2233–2235 (2011).
21. X. Wang, K. Tian, L. Yuan, E. Lewis, G. Farrell, and P. Wang, "A High-Temperature Humidity Sensor Based on a Singlemode-Side Polished Multimode-Singlemode Fiber Structure," *J. Lightwave Technol.* **36**(13), 2730–2736 (2018).
22. W. Lin, Y. Miao, H. Zhang, B. Liu, Y. Liu, and B. Song, "Fiber-optic in-line magnetic field sensor based on the magnetic fluid and multimode interference effects," *Appl. Phys. Lett.* **103**(15), 3285–3287 (2013).

23. Y. Chen, Q. Han, T. Liu, X. Lan, and H. Xiao, "Optical fiber magnetic field sensor based on single-mode-multimode-single-mode structure and magnetic fluid," *Opt. Lett.* **38**(20), 3999–4001 (2013).
24. Y. Liu and L. Wei, "Low-cost high-sensitivity strain and temperature sensing using graded-index multimode fibers," *Appl. Opt.* **46**(13), 2516–2519 (2007).
25. J. Huang, X. Lan, H. Wang, L. Yuan, T. Wei, Z. Gao, and H. Xiao, "Polymer optical fiber for large strain measurement based on multimode interference," *Opt. Lett.* **37**(20), 4308–4310 (2012).
26. K. Tian, G. Farrell, X. Wang, W. Yang, Y. Xin, H. Liang, E. Lewis, and P. Wang, "Strain sensor based on gourd-shaped single-mode-multimode-single-mode hybrid optical fibre structure," *Opt. Express* **25**(16), 18885–18896 (2017).
27. Q. Wang, G. Farrell, and W. Yan, "Investigation on Single-Mode–Multimode–Single-Mode Fiber Structure," *J. Lightwave Technol.* **26**(5), 512–519 (2008).
28. R. Yang, Y.-S. Yu, Y. Xue, C. Chen, Q.-D. Chen, and H.-B. Sun, "Single S-tapered fiber Mach-Zehnder interferometers," *Opt. Lett.* **36**(23), 4482–4484 (2011).
29. H. Y. Choi, M. J. Kim, and B. H. Lee, "All-fiber Mach-Zehnder type interferometers formed in photonic crystal fiber," *Opt. Express* **15**(9), 5711–5720 (2007).
30. K. Tian, G. Farrell, E. Lewis, X. Wang, H. Liang, and P. Wang, "A high sensitivity temperature sensor based on balloon-shaped bent SMF structure with its original polymer coating," *Meas. Sci. Technol.* **29**(8), 085104 (2018).
31. Q. Wang and G. Farrell, "Numerical investigation of multimode interference in a multimode fiber and its applications in optical sensing," in *Photonics Europe*, pp. 327–31, 2006.